

This is the accepted manuscript made available via CHORUS. The article has been published as:

Thermal rectification in restructured graphene with locally modulated temperature dependence of thermal conductivity

Anuj Arora, Takuma Hori, Takuma Shiga, and Junichiro Shiomi

Phys. Rev. B **96**, 165419 — Published 10 October 2017

DOI: [10.1103/PhysRevB.96.165419](https://doi.org/10.1103/PhysRevB.96.165419)

Thermal rectification in restructured graphene with locally modulated temperature dependence of thermal conductivity

Anuj Arora¹, Takuma Hori¹, Takuma Shiga¹, and Junichiro Shiomi^{1,2*}

¹*Department of Mechanical Engineering, The University of Tokyo, 7-3-1 Hongo, Bunkyo, Tokyo, 113-8656, Japan*

²*Center for Materials research by Information Integration, National Institute for Materials Science, 1-2-1 Sengen, Tsukuba, Ibaraki, 305-0047, Japan*

* Email address: shiomi@photon.t.u-tokyo.ac.jp

Abstract

We study thermal rectification (TR) in a selectively restructured graphene by performing deviational phonon Monte Carlo (MC) simulations with frequency-dependent phonon transport properties obtained from first principles. The restructuring is achieved by introducing vacancy defects in a portion of graphene. The defects significantly change phonon transport properties, which results in a modulation of temperature dependence of thermal conductivity. With this modulated temperature dependence, we predict TR ratio through an iterative scheme (IS), where heat flow through the system is analyzed by solving the Fourier's law of heat conduction with spatially varying temperature-dependent thermal conductivity. To identify structure parameters for maximal TR ratio, we investigate the influence of defect size, volume percentage of defects, and system (consisting of defective and non-defective regions) length through IS analysis. As results, we find that TR ratio is mainly a function of length of defective and non-defective regions, and volume percentage of defect, whereas it is mostly independent of defect size. A longer (of the order 10 μm) non-defective side, coupled to a shorter (of the order 100 nm) defective side, can lead to large TR ratios. Finally, MC simulation for the restructured graphene (full system) is performed to verify the predictions from IS analysis. The full system calculations give similar trends but with enhanced TR ratios up to 70% for the temperature range of 200-500 K.

I. Introduction

Thermal rectification (TR) is the phenomenon of directionally preferential heat transport, analogous to electrical transport in an electrical diode. After the experimental demonstration by Starr [1], this phenomenon has gained gradual interest, and numerous experimental and theoretical studies have been performed to get deeper insights into underlying mechanisms [2,3]. Improved understanding facilitates development of devices like thermal transistors, thermal logic circuits, and thermal diodes [4,5] for directional insulation, thermal memory, and computations. Thermal rectification ratio (γ_{TR}) is defined as

$$\gamma_{\text{TR}}(T_0, \Delta T) = \frac{Q_+ - Q_-}{Q_+} (Q_+ > Q_-), \quad (1)$$

where T_0 , ΔT , Q_+ , and Q_- denote mean temperature, temperature difference between hot and cold ends, larger heat current, and smaller heat current in the opposite direction, respectively.

Enhancement for Q_+/Q_- has been commonly considered by introducing a structural asymmetry in the system yielding an asymmetric phonon transport. Till date, mass-loading [6-8], nanostructure embedded interface [9,10], and shape asymmetric tapered (tailored) nanomaterials [10-16] and networks [17] have been studied so far. Measured γ_{TR} values are mostly less than 40% and usually smaller than theoretical predictions (references are therein Ref. [2]).

Contrary to these methods for introducing structural asymmetry, an alternative way to give rise to asymmetric phonon transport is connecting two materials with different temperature-dependence of thermal conductivities. The method has been theoretically proposed [18,19] and experimentally demonstrated ($\gamma_{\text{TR}} \sim 35\%$) [20,21]. Following the reference [18], below we summarize the mechanics underlying the approach: Supposing we have two materials, “1” and “2”, with sufficiently different temperature-dependence of thermal conductivities (κ_1 and κ_2). In comparison to κ_2 , κ_1 is a slowly varying function of T . On applying a temperature gradient from “1” to “2” and assuming that throughout “1” and “2” temperatures are equivalent with the reservoirs’ temperatures ($T_1 = T_H$ and $T_2 = T_C$), thermal conductivities of the two materials exhibit $\kappa_1 = \kappa_1(T_H)$ and $\kappa_2 = \kappa_2(T_C)$, respectively (Fig. 1(a)). On the other hand, for the reverse gradient-direction case (Fig. 1(b)), thermal conductivities similarly exhibit $\kappa_1 = \kappa_1(T_C)$ and $\kappa_2 = \kappa_2(T_H)$. In this case, $\kappa_1(T_H)$ is slightly lower than $\kappa_1(T_C)$ whereas $\kappa_2(T_H)$ is much lower than $\kappa_2(T_C)$. This asymmetric variation, in principle, can lead to thermal rectification. Here, it is noted that connecting two materials with different phonon transport spectra, naturally results in interfacial thermal resistance,

1 which depending on system characteristics could be difficult to exactly determine.

2 Hence, from a practical standpoint, to avoid this added complexity due to resultant interfacial thermal
3 resistance, we realize a graded temperature dependence of thermal conductivity in a single material by
4 restructuring a portion of the material with vacancy defects (Fig. 1(c)). These defects open additional
5 scattering pathways for phonons with comparatively long mean free paths (MFPs), significantly
6 modulating the temperature dependence of thermal conductivity. In achieving TR by restructuring, the
7 potential to introduce a large difference in phonon transport characteristics (or thermal conductivity)
8 between different regions, can play an important role. Therefore, we choose graphene since phonon MFPs
9 in graphene are widely distributed (few nanometers to micrometer scale) and phonons with MFP longer
10 than 500 nm contribute over $2/3^{\text{rd}}$ of the overall thermal conductivity [22,23]. As discussed later, such
11 broad spectrum is preferable for modulating temperature dependence of thermal conductivity at high
12 temperature regime. Besides, for a phonon-defect interaction to seriously impede the phonon transport, its
13 MFP should be at least comparable to the defect size. Therefore, a wider MFP range provides flexibility
14 in deciding the defect size.

15 In this work, performing deviational Monte Carlo simulation with phonon transport properties of
16 graphene obtained from first principles, we investigate the influence of structure parameters such as
17 defect size, volume percentage of defects, lengths of defective and non-defective regions on heat
18 conduction in restructured graphene and evaluate their impact on thermal rectification.

19 The paper is organized as follows. The following section provides computational details. Section III
20 discusses influence of system size and vacancy defects in modulating the temperature dependence of
21 thermal conductivity. Subsequently, we show the results of TR in restructured graphene through IS
22 analysis and full phonon MC simulation. Finally, a conclusion is presented in the last section.

23 24 **II. Method**

25 **II. A. Deviational Monte Carlo (MC) simulation and phonon transport properties of** 26 **graphene**

27 In this work, we employ deviational Monte Carlo (MC) scheme, as proposed by Péraud, *et al.* [24],
28 which has been successfully applied to phonon transport in nanostructured materials [25-28]. The
29 approach is based on the concept of control variates and solves energy-based deviational Boltzmann

1 transport equation (BTE);

$$2 \quad \frac{\partial e^d}{\partial t} + \mathbf{v}_j(\omega) \cdot \nabla_{\mathbf{r}} e^d = \left. \frac{\partial e^d}{\partial t} \right|_{\text{scattering}}, \quad (2)$$

3 where $\mathbf{v}_j(\omega)$ and $\tau_j(\omega)$ denote group velocity and relaxation time of phonon with angular frequency ω and
 4 polarization j . $e^d = e - e^{\text{eq}}(T_{\text{eq}})$ is the deviation in energy distribution from suitably chosen equilibrium
 5 $e^{\text{eq}}(T_{\text{eq}})$. Under single-mode relaxation time (SMRT) approximation, the most commonly used
 6 approximation for solving Eq. (2), the R.H.S. reduces to $(e^{\text{loc}} - e^{\text{eq}}(T_{\text{eq}}) - e^d) / \tau_j(\omega)$, where e^{loc} refers to
 7 the equilibrium distribution corresponding to the local temperature.

8 These MC simulations require frequency-dependent phonon properties such as density of states,
 9 group velocity, and phonon relaxation time as input. To obtain these quantities, we perform anharmonic
 10 lattice dynamics (ALD) with interatomic force constants (IFCs) of graphene. Here, IFCs describe
 11 interactions among atoms in crystal and are defined as the Taylor expansion coefficients of potential
 12 energy V with respect to atomic displacement u :

$$13 \quad -\frac{\partial V}{\partial u_i^\alpha} = -\sum_{j,\beta} \Phi_{ij}^{\alpha\beta} u_j^\beta - \frac{1}{2} \sum_{jk,\beta\gamma} \Psi_{ijk}^{\alpha\beta\gamma} u_j^\beta u_k^\gamma + \dots, \quad (3)$$

14 where i, j, k are atomic indices, α, β, γ are Cartesian coordinates. Φ and Ψ are harmonic and third-order
 15 anharmonic IFCs, respectively.

16 Harmonic IFCs are obtained by using density functional perturbation theory (DFPT) implemented in
 17 the *Quantum Espresso* package [29]. In the self-consistent calculation for electrons, 32×32
 18 Monkhorst-Pack uniform k -mesh [30] is used to sample electric states in the first Brillouin zone. Cutoff
 19 energies for plane wave expansion and charge density are set to 55 and 440 Ryd, respectively. Ultrasoft
 20 non-relativistic pseudopotential is chosen, and local density approximation is used to describe
 21 exchange-correlation effect. Lattice constant of graphene is set to 2.445 Å in this work. In DFPT
 22 calculations for phonons, 32×32 uniform q -mesh is employed to calculate harmonic IFCs.

23 Once harmonic IFCs are obtained, phonon dispersion relation is readily obtained by solving a
 24 dynamical matrix with given wavevector. Figure 3(a) shows the calculated dispersion relation of graphene
 25 along different high symmetry lines. It is seen that long-range harmonic IFCs are required to obtain the
 26 dispersion relation in agreement with experiments [31,32]. While frequency-dependent density of states
 27 and group velocities are obtained from the dispersion relation, phonon relaxation time require anharmonic

1 calculations.

2 Third-order anharmonic IFCs are extracted using an open source code *thirdorder.py* [33] from the
3 force-displacement data obtained from density functional theory calculations, using *Quantum Espresso*.
4 The force-displacement dataset is obtained through finite displacement method, in the
5 primitive-unit-cell-based 5×5 supercell with 50 atoms. The range of third-order anharmonic IFCs is kept
6 to fifth nearest neighbors, necessary for calculating phonon transport properties of graphene [22,34].

7 Now, SMRT approximation is inadequate for investigating phonon transport in graphene [35] since it
8 substantially overestimates umklapp scattering, underestimating thermal conductivity. Therefore, we
9 perform ALD calculations with iterative solution [33,36] to BTE using *ShengBTE* [33]. Figure 3(b) shows
10 calculated thermal conductivity of pristine graphene compared to previous calculations [22,37] and
11 experiments [38-40]. For ALD, we use 200×200 uniform q -mesh. In Fig. 3(b), results for MC simulations
12 of pristine graphene with phonon transport properties obtained from ALD calculations are also presented.
13 There is a reasonable agreement with reported calculations and experiments [22,37-40].

14 Regarding the discrepancy in calculated thermal conductivity values between present and previous
15 studies, the employed iterative scheme, no longer provides relaxation time, as it calculates deviation in
16 phonon distribution function (δn_q) from the equilibrium distribution (n_q); $\delta n_q = -\mathbf{F}_q \cdot \nabla T (\partial n_q / \partial T)$ [33]. \mathbf{F}_q is
17 a non-equilibrium quantity with the dimension of length (physically same as MFP) and includes
18 contribution from non-equilibrium distribution of other phonons involving three-phonon scattering. After
19 calculating \mathbf{F}_q , relaxation time is obtained as $\tau_q = -\mathbf{F}_q \cdot \mathbf{v}_q / |\mathbf{v}_q|^2$. Depending on \mathbf{F}_q , τ_q can be positive or
20 negative. However, the present MC framework requires positive τ_q to implement probabilistic
21 phonon-phonon scattering. Hence, we enforce positive signs for all τ_q , that is, use absolute τ_q , converted
22 from \mathbf{F}_q (Fig. 3(c)). Through MC simulations of various systems (defective and non-defective), it is
23 ascertained that the phonons with originally negative τ_q , contribute merely 5-10% to overall thermal
24 conductivity. With a relatively low contribution of these phonon modes, we can safely assume that by
25 enforcing absolute τ_q , the effect on subsequent calculations is insignificant. This is clear from the accurate
26 reproduction of accumulation functions of thermal conductivity (Fig. 3(d)) obtained by ALD, and MC
27 simulations using phonon transport properties from ALD.

28 Utilizing these frequency and mode dependent phonon properties, phonon MC simulations can be
29 performed. Since the method details are well explained in [24], we only briefly introduce the process flow.
30 In the method, phonon advection and scattering is simulated iteratively. Advection speed of a phonon
31 corresponds to its mode dependent group velocity. Within the advection step, phonon-defect scattering is

also simulated. In the simulation, defects are represented as ‘no-go’ regions of given shape and size. On reaching the defect boundary, phonon direction is reassigned as per the 2D version of diffuse reflection model [41,42] following Lambert’s cosine law. It is realized by generating a random number $R \in (-1, 1)$ and setting $\theta = \arcsin R$, where θ is the transport direction angle with respect to the boundary normal. The same randomization is employed for emission boundary. Following the advection step, phonon propagation direction is randomly reoriented depending on the relaxation time based probability to imitate phonon-phonon scattering. Finally, to eliminate edge effect (Fig. 1(c)), unit cell boundary along y is set to be periodic. For x -direction, either isothermal or periodic unit cell boundary condition [24,43] is prescribed to impose the intended heat flux. For example, in the pristine case, we apply periodic unit cell boundary conditions along x -direction.

Two sets of calculations are done with these simulations. First, referred as MC simulations, to determine the temperature dependent thermal conductivity at a given temperature T_{eq} ; system ends are maintained at $T_{eq} + \Delta T$ and $T_{eq} - \Delta T$ ($\Delta T = 0.01$ K). Second set, referred as full-MC simulations, is to quantify the rectification performance of the actual system, consisting of both defective and non-defective regions, for larger temperature difference ($T_{eq} = 350$, $\Delta T = 150$ K). In these calculations, for an accurate implementation of temperature-dependent phonon transport properties, whole temperature range is divided into smaller bins ($dT = 50$ K). For each bin, a power law relation capturing relaxation time variation with temperature is defined (Eq. 4), where $\tau_{i,0}$ is phonon relaxation time for a given frequency and vibrational mode, in i th material at mean temperature, $T_0 = (T_H + T_C)/2$.

$$\tau_i(T) = \tau_{i,0}(T/T_0)^{n_i}, \quad (4)$$

Here, power law exponent (n) is estimated by fitting (approximately) a straight line through the log-log plot for κ v/s T . The slope of this fit gives n ,

$$\kappa_i(T) = \kappa_{i,0}(T/T_0)^{n_i}, \quad (5)$$

These simulations are continued until there is no appreciable change in the temperature distribution over physical simulation time of several nanoseconds, a function of system size and defect number. The effective thermal conductivity is evaluated from the calculated **heat flux Q , using Eq. 6.**

$$\kappa_{eff} = \left(\frac{Q}{L_y L_z} \right) \left(\frac{\Delta T}{L_x} \right)^{-1}, \quad (6)$$

here, thickness of L_z is set to 0.34 nm, same as the van der Waals thickness.

II. B. Estimation of thermal rectification ratio through Iterative Scheme (IS)

The systems examined in this study (Fig. 1(c)) include several parameters such as length of

1 non-defective graphene (L_{ND}), length of defective graphene (L_{D}), defect size (l_{d}), and volume percentage
 2 of defects (ϕ). Therefore, it is computationally expensive to identify the optimal structure with maximum
 3 TR by simulating all possible parameter combinations through full-MC simulation. Therefore, we employ
 4 the IS analysis to predict γ_{TR} of restructured graphene by following the procedure described in Fig. 2.
 5 First, we divide the restructured graphene into non-defective and defective regions, and separately
 6 calculate temperature-dependent thermal conductivities for the two regions. Further, each region is
 7 sub-divided into smaller segments. Assuming one-dimensional heat flow, heat flux (Q_x) through a
 8 segment at position x is given by

$$Q_x = \kappa_x A_x (\Delta T_x / L) \quad (7)$$

10 with L , A_x and $\kappa_x \equiv \kappa_x(T_x)$ being the segment length, area of cross-section, and thermal conductivity at
 11 position x , respectively. For the temperature dependence of thermal conductivity, we used the form
 12 prescribed in Eq. (5). After obtaining Q_x for each segment, an average heat flux $Q_{\text{ave/Forward}}$ is calculated.
 13 Subsequently, using this average heat flux, $Q_{\text{ave/Forward}}$ for the whole domain, temperature distribution is
 14 recalculated with Eq. (7), fixing the domain end-walls' temperatures at T_{L} and T_{R} . Finally, for the new
 15 temperature distribution, local thermal conductivity, κ_x is recalculated and the procedure is repeated until
 16 a convergence is achieved for $Q_{\text{ave/Forward}}$. In full-MC calculations, system-of-interest has a smooth
 17 transition from a defective to non-defective region. Therefore, for consistency, we assume a zero
 18 interfacial thermal resistance in IS analysis. Similarly, we calculate $Q_{\text{ave/Backward}}$ for reverse temperature
 19 gradient and estimate γ_{TR} with Eq. (1).

20 An identical theoretical approach has been proposed by C. Dames [18] for evaluating the performance
 21 of thermal rectifiers. Through his analysis, γ_{TR} for the combined system is given by,

$$\gamma_{\text{TR}} = \left[\frac{n_1 - n_2}{(\rho^{1/2} + \rho^{-1/2})^2} \Delta \right] \cdot \left[1 - \frac{n_1 - n_2}{2(\rho^{1/2} + \rho^{-1/2})^2} \Delta \right]^{-1}, \quad (8)$$

23 where $\Delta = (T_{\text{L}} - T_{\text{R}})/T_0$ and ρ are dimensionless temperature bias and thermal resistance ratio, respectively
 24 and are defined as

$$\rho = \frac{R_{2,0}}{R_{1,0}}, R_{i,0} = \frac{L_i}{\kappa_{i,0} A_i}, \quad (9)$$

26 On further simplification, retaining only leading order term in Δ to yield

$$\gamma_{\text{TR}} = \left[\frac{n_1 - n_2}{(\rho^{1/2} + \rho^{-1/2})^2} \right] \Delta, \quad (10)$$

Δ in our simulation for the temperature range of 200-500 K is around 0.86 and exceeds the value ($\Delta \sim 0.1$) for which Eq. (10) is valid. Hence, this expression cannot be directly used for evaluating γ_{TR} . However, it still provides important insights for qualitative understanding of the effects of different parameters. It can be seen that, for maximizing γ_{TR} , difference in power-law exponent ($n_1 - n_2$) should be enhanced and thermal resistance ratio (ρ) should be equal (or close) to 1.0 (impedance matching).

III. Results and Discussions

III. A. Modulation of temperature dependence of thermal conductivity

Figures 4(a) and 4(c) show temperature-dependent thermal conductivities of finite-length graphenes with and without defects, respectively. In the calculations, we use isothermal unit cell boundary condition [24,44] along heat current (x) direction. With decreasing system size (L_D or L_{ND}) and increasing ϕ , boundary and defect scatterings increase, leading to a greater reduction in thermal conductivity from the pristine value. Besides, these extrinsic scatterings largely modulate temperature dependence of thermal conductivity, which results in an increasingly positive n_i . These observations arise due to a weakening role of intrinsic temperature-dependence as phonon-phonon scattering gets less dominant than phonon-boundary and/or phonon-defect scattering. In theory, temperature dependence of thermal conductivity at low temperature regime (in comparison to the Debye temperature, ~ 2300 K [45] for graphene) is mainly determined by that of heat capacity. Extrinsic scattering strongly suppress contributions of longer MFP (low frequency) phonons to heat conduction and increase relative contributions of short MFP (high frequency) phonons, as is clearly seen in Figs. 4(b) and 4(d). This fact suggests that increasing $n_1 - n_2$ is correlated with γ_{TR} (Eq. (10)), and larger L_{ND} , smaller L_D , and higher ϕ are desirable. However, the restructuring can also lead to larger impedance mismatch ($\rho \gg 1$ or $1 \ll \rho$), therefore, it is important to explore the combination of defective and non-defective graphenes, balancing the two competing factors ($n_1 - n_2$, and ρ).

We also analyze the modulation effect due to size and shape of defect. Figure 5(a) shows temperature-dependent thermal conductivity of defective graphenes for three different defect sizes (l_d)

(constant ϕ and L_D). For a fixed ϕ , larger l_d means fewer defects and a smaller surface area. Since, the interaction between phonon and defect is qualitatively proportional to defect surface area, larger l_d lowers the phonon-defect scattering probability, which is highlighted by a smaller n_i and higher κ for larger l_d . As for the defect shape, comparing circle and square shapes for the same defect percentage, it is found that defect shape has no additional effect on κ - T characteristics (Fig. 5(b)). Thus, we only consider square defects.

III. B. Thermal rectification in restructured graphene

Analysis in the previous section suggests that a combination of small L_D and relatively larger L_{ND} is preferable for large n_1 - n_2 and high rectification. To quantify this, firstly we calculate γ_{TR} for several L_{ND} by IS analysis. Figure 6(a) shows L_{ND} -dependence of γ_{TR} for different ϕ ($=4, 9, 16$, and 25%). Here L_D and l_d are fixed to 100 nm and 5 nm, respectively. For any ϕ , with increasing L_{ND} , γ_{TR} increases and then decreases. The trend can be understood in terms of the L_{ND} -dependences of n_1 - n_2 and ρ (Figs. 6(b) and 6(c)). Since, L_D is fixed, n_D and κ_D are constants whereas n_{ND} (κ_{ND}) monotonically decreases (increases) with increasing L_{ND} and saturates to pristine values in the end. Similarly, n_D - n_{ND} (n_1 - n_2) increases and saturates at large enough L_{ND} (Fig. 6(b)). Meanwhile, since ρ is proportional to L_{ND}/κ_{ND} , ρ increases with L_{ND} (Fig. 6(c)). Ultimately, for large L_{ND} , ρ deviates from impedance matching ($\rho=1$), with the resistance of the non-defective side becoming significantly higher than that of defective side. Therefore, the two competing factors (n_D - n_{ND} , and ρ) indicate that larger L_{ND} does not necessarily lead to higher γ_{TR} . However, looking at Figure 6 (a), for a constant L_D and l_d , a larger- L_{ND} system achieves a higher maximum γ_{TR} (γ_{TR}^{\max}) for a correspondingly higher ϕ . This justifies the selection of larger L_{ND} for maximizing rectifier performance.

Similarly, we calculate γ_{TR} for several values of L_D . Figure 7(a) shows L_D -dependent γ_{TR} for different ϕ ($=1, 9, 16, 25$, and 36%). Here L_{ND} and l_d are fixed to 25 μ m and 5 nm, respectively. A general trend is seen, such that for any ϕ , with increasing L_D , γ_{TR} increases and then decreases. Since L_{ND} is fixed, n_{ND} and κ_{ND} are constants, whereas n_D (κ_D) monotonically decreases (increases) with increasing L_D . Further, n_D and κ_D approach to pristine system values. Correspondingly, n_D - n_{ND} (n_1 - n_2) (Fig. 7(b)) decreases. Meanwhile, ρ being proportional to κ_D/L_D , at large L_D , ρ diverges from the impedance matching ($\rho=1$)

(Fig. 7(c)). As such, resistance of the defective side becomes significantly higher than that of non-defective side. Similar to the effect of increasing L_{ND} , the two competing factors (n_D - n_{ND} and ρ) determine the γ_{TR} trend. Therefore, smaller L_D does not always increase γ_{TR} . However, for a given L_{ND} and l_d (Fig. 7(a)), γ_{TR}^{\max} grows with increasing ϕ and the corresponding L_D for achieving γ_{TR}^{\max} becomes smaller, making ‘smaller L_D ’ an appropriate choice for maximizing the rectifier performance. Hence, combining these observations, to maximize γ_{TR} , we need a combination of large L_{ND} and small L_D . True to this conclusion, it is seen that out of all the tested combinations for IS analysis, the maximum observed γ_{TR} value ($\sim 60\%$) is obtained for the case with $L_{ND} = 20 \mu\text{m}$ (largest tried L_{ND} value) and $L_D = 100\text{nm}$ (smallest tried L_D value) at $\phi = 36\%$.

Next, in Fig. 8(a), the variation of γ_{TR} with l_d is studied (fixed L_D and L_{ND}). As seen, γ_{TR}^{\max} is almost insensitive to l_d . However, the corresponding ϕ for γ_{TR}^{\max} is larger for larger l_d (indicated by the black dotted ellipse in Fig. 8(a)). This follows the discussion on effect of changing l_d (section III. A.). Extending that discussion, we see that by careful adjustment of ϕ with changing defect size, κ - T characteristics for the defective side remain almost unaffected (Fig 8(b)). Hence, for a given $(L_D + L_{ND})$ system, there is no enhancement in the peak rectification characteristics with change in l_d .

We have so far evaluated the impact of each parameter on γ_{TR} by IS analysis. In the remaining part, we perform full-MC simulation for the cases with large γ_{TR} to verify the predictions from the IS analysis. Hereafter, we define γ_{TR} obtained by full-MC simulation and IS approach as γ_{TR}^{MC} and γ_{TR}^{IS} , respectively. Figure 9(a) shows ϕ -dependent γ_{TR}^{MC} and γ_{TR}^{IS} for different L_{ND} . In these simulations, L_D and l_d are respectively fixed to 100 nm and 5 nm. A significant difference between full-MC and IS analysis is that the latter uses an approximate power-law temperature dependence of thermal conductivity (section II. A.). This conductivity-temperature relation is obtained by imposing a small temperature gradient whereas full-MC incorporates much larger temperature gradients in the system. This helps to capture the non-equilibrium of the phonon population in actual systems. Hence, even though the shape of γ_{TR}^{IS} trend agrees well with that of γ_{TR}^{MC} , some discrepancies between γ_{TR}^{MC} and γ_{TR}^{IS} are seen.

As seen in Fig. 9(b), $\gamma_{TR}^{\text{MC}} / \gamma_{TR}^{\text{IS}}$ monotonically decreases with increasing ϕ , although it is almost constant for shorter L_{ND} ($\sim 10 \mu\text{m}$). Relatively high $\gamma_{TR}^{\text{MC}} / \gamma_{TR}^{\text{IS}}$ at larger L_{ND} is attributed to phonon dynamics near the interface (Fig 10(a)). In the IS analysis, as the defective and non-defective regions are treated separately, scattering rates for the phonons approaching the interface increase (Fig 10(b)). This affects the already highly-non-equilibrium phonon distribution, due to ballistic phonon interaction with

1 the defects and side boundaries. Addition of non-defective region, to the defective system, in full-MC
 2 simulation, reduces these interactions for some phonons. However, longer-MFP phonon continue to
 3 interact with the interface (Fig. 10(c) & (d)). This creates a discrepancy between the phonon dynamics in
 4 the two analyses. Moreover, as mentioned before, phonon MFP range in graphene is considerably large
 5 and with increase in L_{ND} , an increasing number of phonons can avoid this interface-interaction, enhancing
 6 the discrepancy between the two analyses. Further, due to finite MFP range, we expect this increase in
 7 discrepancy to saturate for a big enough L_{ND} .

8 Returning to Fig. 9, since γ_{TR}^{MC} and γ_{TR}^{IS} maximizes at almost the same ϕ , a higher $\gamma_{TR}^{MC} / \gamma_{TR}^{IS}$ is
 9 mainly attributed to n_1 - n_2 . In calculating γ_{TR}^{IS} , we divide the restructured graphene into defective and
 10 non-defective regions and obtain n_1 , n_2 , κ_1 and κ_2 (Eq. (5)) separately. On the contrary, in full-MC
 11 simulation, there is a smooth transition from defective to non-defective region. As such, there is no
 12 distinct interface, indicating that phonons propagating in non-defective region can pass through the
 13 interface without scattering. Consequently, actual n_2 will be more negative than the one used in IS
 14 approach (i.e. $n_2^{MC} < n_2^{IS}$). On the other hand, phonon-defect scattering is still dominant for phonon
 15 transport in defected region and is not affected much by presence or absence of interface, thus, one can
 16 assume $n_1^{MC} \sim n_1^{IS}$. This is clearly seen from the fact that $\gamma_{TR}^{MC} / \gamma_{TR}^{IS}$ approaches to 1.0 as ϕ increases (Fig.
 17 9(b)). Consequently, the discrepancy between full-MC simulation and IS analysis becomes small for
 18 larger defect concentrations.

19 Lastly, a comment on a few limitations of the full-MC simulations carried out in this study. (i)
 20 Calculated κ_{eff} , which determine γ_{TR}^{MC} , is sensitive to local temperature distribution as it affects local
 21 phonon transport properties. Hence, it requires a fine mesh of unit cells to precisely capture the
 22 distribution but too fine a mesh is computationally expensive. Hence, we sacrifice some accuracy to keep
 23 the computational requirements within practical limits. (ii) Further, graphene being a 2-D material, has
 24 very strict selectivity [46] (excludes all phonon processes involving odd number of phonons from ZA and
 25 ZO mode) for three-phonon scattering. However, in present simulations while implementing
 26 phonon-phonon scattering, though this selectivity has been accounted in ALD calculations, it is not
 27 directly implemented in MC and full-MC simulations. Hence, given the differences between IS and
 28 full-MC simulation, we expect a higher TR ratio enhancement from the latter but these limitations can

1 potentially reduce that difference.

2 However, despite these limitations, with the advantages of the current formulation, the calculated
3 values are a good estimate for $\gamma_{\text{TR}}^{\text{MC}}$. Further, with present technology, we can realize and study the
4 proposed systems [47,48]. Hence, it will be interesting to have a comparative experimental analysis to
5 verify these results and gain insights into exploiting this approach for improving rectifier performance.

6

7 **IV. Conclusions**

8 In this work, performing energy-based deviational MC simulation with phonon properties obtained
9 from first principles, we have evaluated thermal conductivity of restructured graphene. As expected,
10 thermal conductivity shows a significant dependence on system parameters like external dimensions, and
11 defect characteristics. Due to wide range of phonon MFPs (multiscale character), nanostructures impede
12 phonon transport and suppress the thermal conductivity. From the obtained temperature versus thermal
13 conductivity trends, we perform IS analysis to estimate the rectifier's performance. Further, we identify
14 optimum parameters for best TR ratios. Consequentially, we conclude that restructuring enhances TR
15 effect, due to successful enhancement of difference in phonon transport characteristics between different
16 regions.

17 Moreover, we see that the peak performance with respect to defect percentage, for a given
18 combination of defective and non-defective side length, is independent of the defect size. Equipped with
19 the knowledge from IS analysis, we have performed full-MC simulations for the optimum parameters,
20 along with few other systems, to verify the trends and identify the differences between IS and full
21 simulations, with highest obtained rectification ratios being in the range of ~60-70%.

1 **Acknowledgements**

2 This work was partially supported by KAKENHI (Grant Numbers 16H04274, 15K17982) and MI²I:
3 "Materials research by Information Integration" Initiative program supported by Japan Science and
4 Technology Agency. This work was performed using facilities of the Institute for Solid State Physics, the
5 University of Tokyo, and the TSUBAME2.0 supercomputer in the Tokyo Institute of Technology
6 supported by the MEXT Open Advanced Research Facilities Initiative.

References

- [1] C. Starr, *Journal of Applied Physics* **7**, 15 (1936).
- [2] N. A. Roberts and D. G. Walker, *International Journal of Thermal Sciences* **50**, 648 (2011).
- [3] M. A. Shiqian Hu, Nuo Yang, and Baowen Li, (May 2016).
- [4] N. Li, J. Ren, L. Wang, G. Zhang, P. Hänggi, and B. Li, *Reviews of Modern Physics* **84**, 1045 (2012).
- [5] Q. Song, M. An, X. Chen, Z. Peng, J. Zang, and N. Yang, *Nanoscale* **8**, 14943 (2016).
- [6] C. W. Chang, D. Okawa, A. Majumdar, and A. Zettl, *Science* **314**, 1121 (2006).
- [7] C.-L. Chiu, C.-H. Wu, B.-W. Huang, C.-Y. Chien, and C.-W. Chang, *AIP Advances* **6**, 121901 (2016).
- [8] A. Mohammad, A. Elena, C. B. Michael, and M.-P. Florian, *Nanotechnology* **20**, 115704 (2009).
- [9] J. Miller, W. Jang, and C. Dames, 317 (2009).
- [10] Y. Wang, S. Chen, and X. Ruan, *Applied Physics Letters* **100**, 163101 (2012).
- [11] N. Yang, G. Zhang, and B. Li, *Applied Physics Letters* **93**, 243111 (2008).
- [12] Z.-G. Shao, B.-q. Ai, and W.-R. Zhong, *Applied Physics Letters* **104**, 013106 (2014).
- [13] S. Ju and X. Liang, *Journal of Applied Physics* **112**, 024307 (2012).
- [14] W. Gang and L. Baowen, *Journal of Physics: Condensed Matter* **20**, 175211 (2008).
- [15] Y. Wang, A. Vallabhaneni, J. Hu, B. Qiu, Y. P. Chen, and X. Ruan, *Nano Letters* **14**, 592 (2014).
- [16] J. Hu, X. Ruan, and Y. P. Chen, *Nano Letters* **9**, 2730 (2009).
- [17] X. Yang, D. Yu, B. Cao, and A. C. To, *ACS Applied Materials & Interfaces* **9**, 29 (2017).
- [18] C. Dames, *Journal of Heat Transfer* **131**, 061301 (2009).
- [19] S.-i. Tamura and K. Ogawa, *Solid State Communications* **152**, 1906 (2012).
- [20] D. Sawaki, W. Kobayashi, Y. Moritomo, and I. Terasaki, *Applied Physics Letters* **98**, 081915 (2011).
- [21] W. Kobayashi, Y. Teraoka, and I. Terasaki, *Applied Physics Letters* **95**, 171905 (2009).
- [22] G. Fugallo, A. Cepellotti, L. Paulatto, M. Lazzeri, N. Marzari, and F. Mauri, *Nano Letters* **14**, 6109 (2014).
- [23] H. Zhang, C. Hua, D. Ding, and A. J. Minnich, *Scientific Reports* **5**, 9121 (2015).
- [24] J.-P. M. Péraud and N. G. Hadjiconstantinou, *Physical Review B* **84**, 205331 (2011).
- [25] W. Tian and R. Yang, *Journal of Applied Physics* **101**, 054320 (2007).

- [26] J. Randrianalisoa and D. Baillis, Journal of Applied Physics **103**, 053502 (2008).
- [27] T. Hori, G. Chen, and J. Shiomi, Applied Physics Letters **104**, 021915 (2014).
- [28] Q. Hao, G. Chen, and M.-S. Jeng, Journal of Applied Physics **106**, 114321 (2009).
- [29] G. Paolo *et al.*, Journal of Physics: Condensed Matter **21**, 395502 (2009).
- [30] H. J. Monkhorst and J. D. Pack, Physical Review B **13**, 5188 (1976).
- [31] J. Maultzsch, S. Reich, C. Thomsen, H. Requardt, and P. Ordejón, Physical Review Letters **92**, 075501 (2004).
- [32] M. Mohr, J. Maultzsch, E. Dobardžić, S. Reich, I. Milošević, M. Damnjanović, A. Bosak, M. Krisch, and C. Thomsen, Physical Review B **76**, 035439 (2007).
- [33] W. Li, J. Carrete, N. A. Katcho, and N. Mingo, Computer Physics Communications **185**, 1747 (2014).
- [34] N. Mingo, K. Esfarjani, D. A. Broido, and D. A. Stewart, Physical Review B **81**, 045408 (2010).
- [35] L. Lindsay, W. Li, J. Carrete, N. Mingo, D. A. Broido, and T. L. Reinecke, Physical Review B **89**, 155426 (2014).
- [36] M. Omini and A. Sparavigna, Physical Review B **53**, 9064 (1996).
- [37] C. D. Landon and N. G. Hadjiconstantinou, Journal of Applied Physics **116**, 163502 (2014).
- [38] S. Chen *et al.*, ACS Nano **5**, 321 (2011).
- [39] S. Chen, Q. Wu, C. Mishra, J. Kang, H. Zhang, K. Cho, W. Cai, A. A. Balandin, and R. S. Ruoff, Nat Mater **11**, 203 (2012).
- [40] J.-U. Lee, D. Yoon, H. Kim, S. W. Lee, and H. Cheong, Physical Review B **83**, 081419 (2011).
- [41] M.-S. Jeng, R. Yang, D. Song, and G. Chen, Journal of Heat Transfer **130**, 042410 (2008).
- [42] B. T. Wong, M. Francoeur, and M. Pinar Mengüç, International Journal of Heat and Mass Transfer **54**, 1825 (2011).
- [43] R. Yang and G. Chen, Physical Review B **69**, 195316 (2004).
- [44] S. Mazumder and A. Majumdar, Journal of Heat Transfer **123**, 749 (2001).
- [45] V. K. Tewary and B. Yang, Physical Review B **79**, 125416 (2009).
- [46] L. Lindsay, D. A. Broido, and N. Mingo, Physical Review B **82**, 115427 (2010).
- [47] H. Wang *et al.*, Scientific Reports **6**, 21823 (2016).
- [48] J. Buchheim, R. M. Wyss, I. Shorubalko, and H. G. Park, Nanoscale **8**, 8345 (2016).

Figures

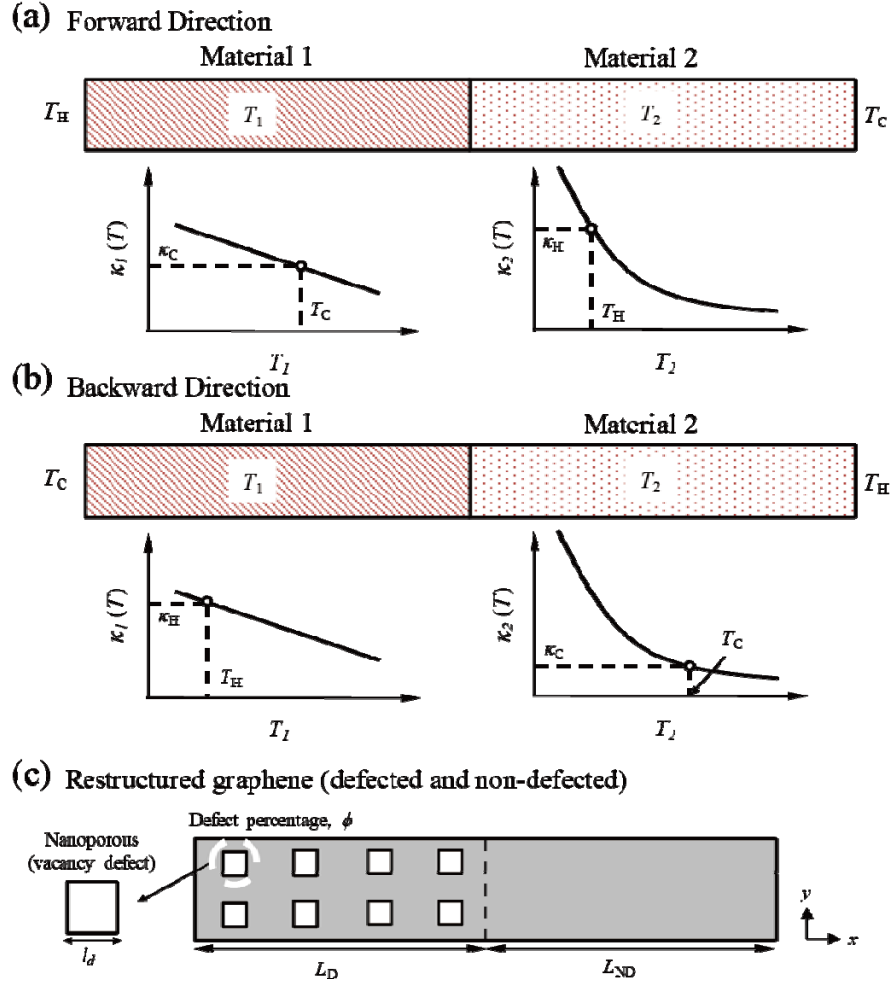


Fig. 1 (a) A system showing a combination of two materials with different temperature-dependent thermal conductivities. Material 1 is connected with hot end whereas material 2 is connected to cold end. (b) Vice versa of (a). (c) Restructured graphene considered in this work. ϕ represents volume percentage of defects. L_D , L_{ND} , and l_d are lengths of defected graphene, non-defected graphene, and defect, respectively. x and y axes are prescribed along the length and width, respectively of the shown graphene system.

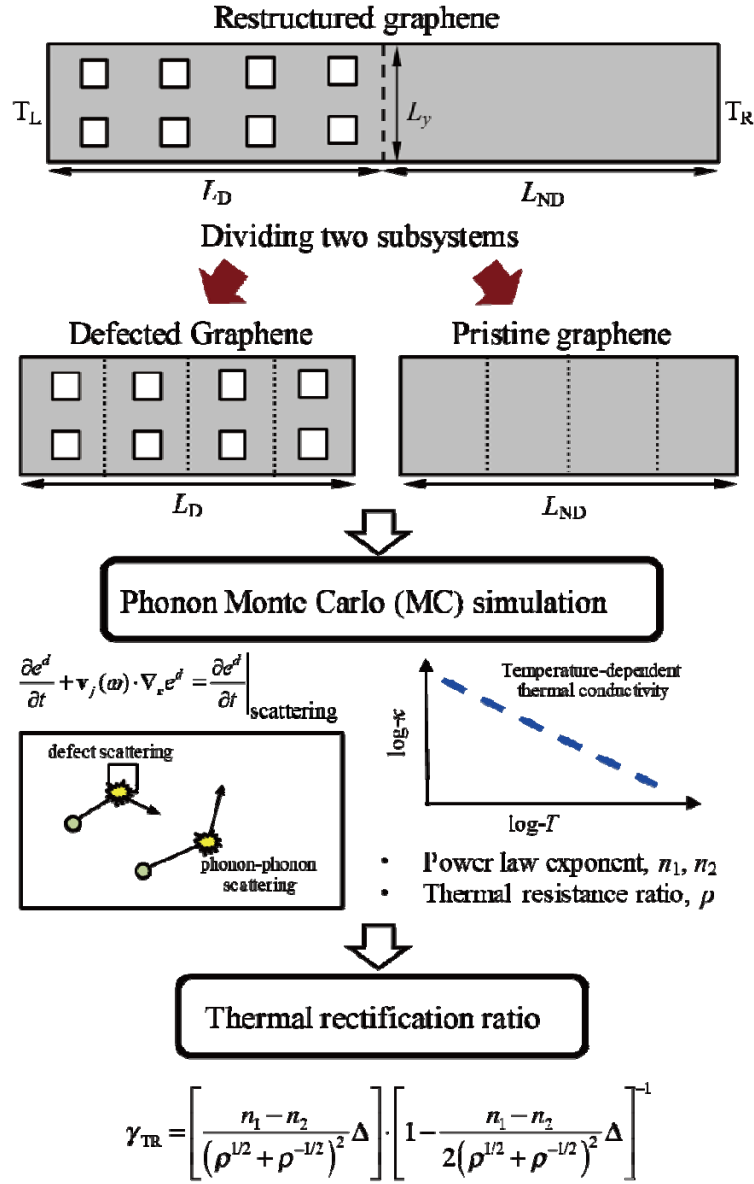


Fig. 2 Schematics for the procedure of evaluation of thermal rectification ratio (γ_{TR}). Firstly phonon transport properties in defective and non-defective graphenes are separately calculated by phonon Monte Carlo (MC) simulation. After the calculation, power-law exponent (n_i) of the i th material is estimated from obtained temperature-dependent thermal conductivity in the temperature range of 200-500 K, where $i=1$ and $i=2$ denote defective and non-defective graphenes, respectively. Thermal rectification ratio (γ_{TR}) is evaluated through IS analysis at the reference temperature ($T_0=350$ K). Dotted lines in the divided subsystems represent their sub-division into smaller segments for IS analysis.

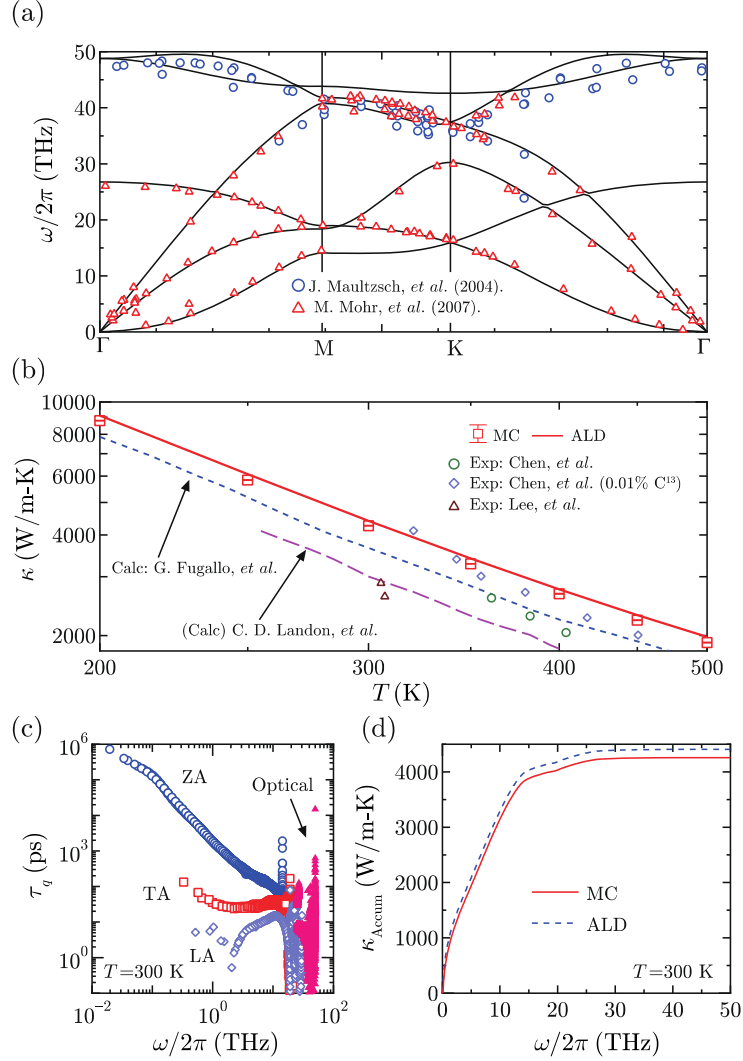


Fig. 3 (a) Phonon dispersion relation of graphene calculated from density functional perturbation theory implemented in the *Quantum Espresso* package [29]. Red open circle and blue square are inelastic x-ray scattering experiments [31,32]. (b) Temperature-dependent thermal conductivity, $\kappa(T)$, of pristine graphene calculated by anharmonic lattice dynamics (ALD) with *ShengBTE* [33] and deviational Monte Carlo (MC) simulation. Solid lines are reported calculations [22,37] and open marks are experiments [38-40]. (c) Frequency-dependent phonon relaxation time (τ_q) of pristine graphene at $T=300$ K obtained from ALD. LA denotes the longitudinal acoustic mode. TA and ZA are in-plane and out-of-plane transverse acoustic modes. (d) Accumulation functions of thermal conductivity spectra at $T=300$ K calculated from ALD and MC.

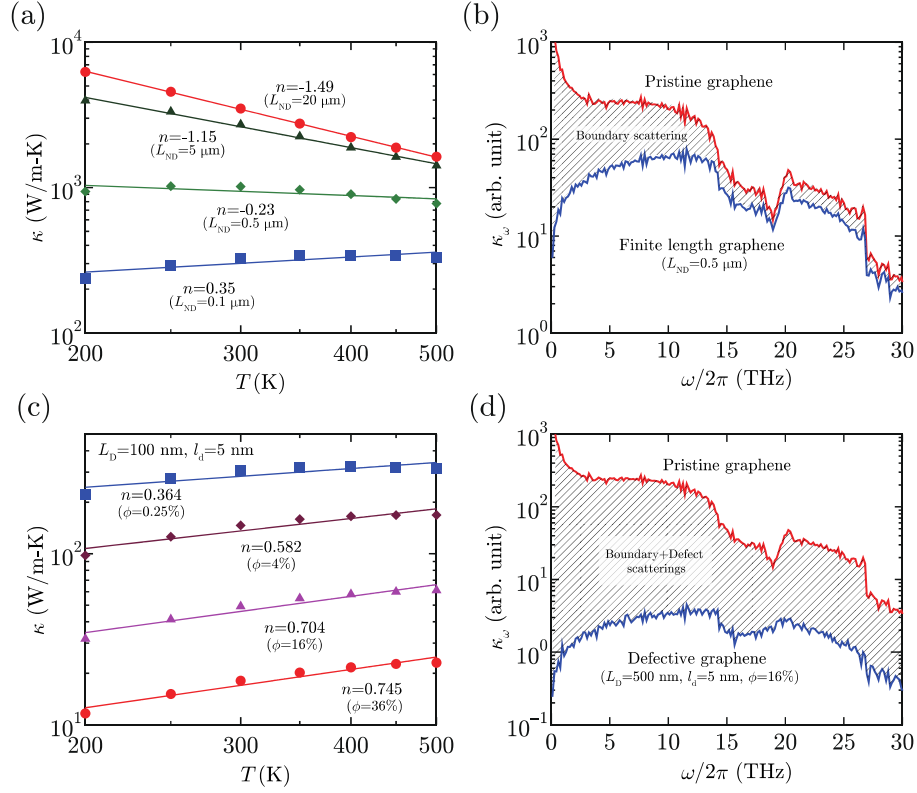


Fig. 4 (a) Temperature-dependent thermal conductivity (κ) of non-defective and defective graphenes with finite lengths (L_{ND} and L_D). Solid lines indicate power-law fitting of κ with respect to temperature, and n denotes the power law exponent for the fitting. (b) Thermal conductivity spectra for pristine graphene and finite-length graphene ($L_{ND} = 0.5 \mu\text{m}$) at $T = 300 \text{ K}$. (c) Temperature-dependent κ of defective graphenes with several volume percentages of defects (ϕ). In the calculation, L_{ND} and l_d are fixed as 100 nm and 5 nm , respectively. (d) Thermal conductivity spectra for pristine graphene and defective graphene ($L_D = 500 \text{ nm}$, $l_d = 5 \text{ nm}$, $\phi = 16\%$) at $T = 300 \text{ K}$.

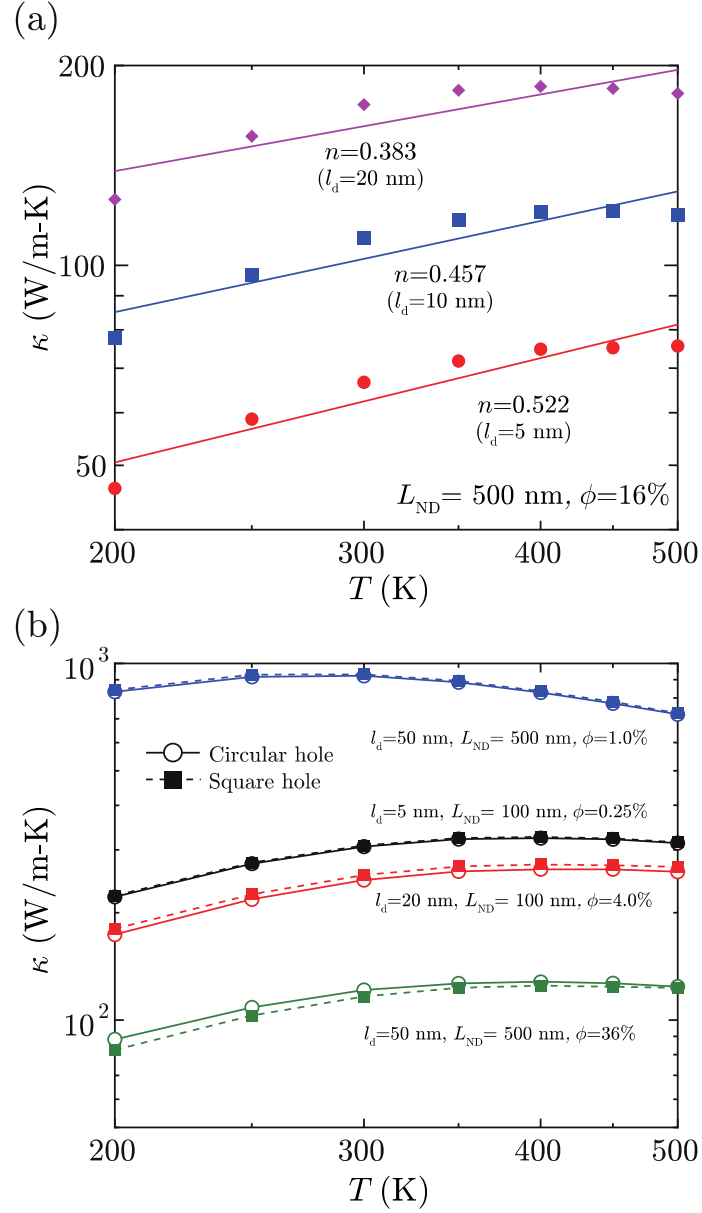


Fig. 5 (a) Temperature-dependent κ of defective graphenes with three different l_d . Here L_D and ϕ are fixed as 500 nm and 16%, respectively. (b) Temperature-dependent κ of defective graphenes with different types of defect. Open circles and filled squares represent circular and square holes, respectively.

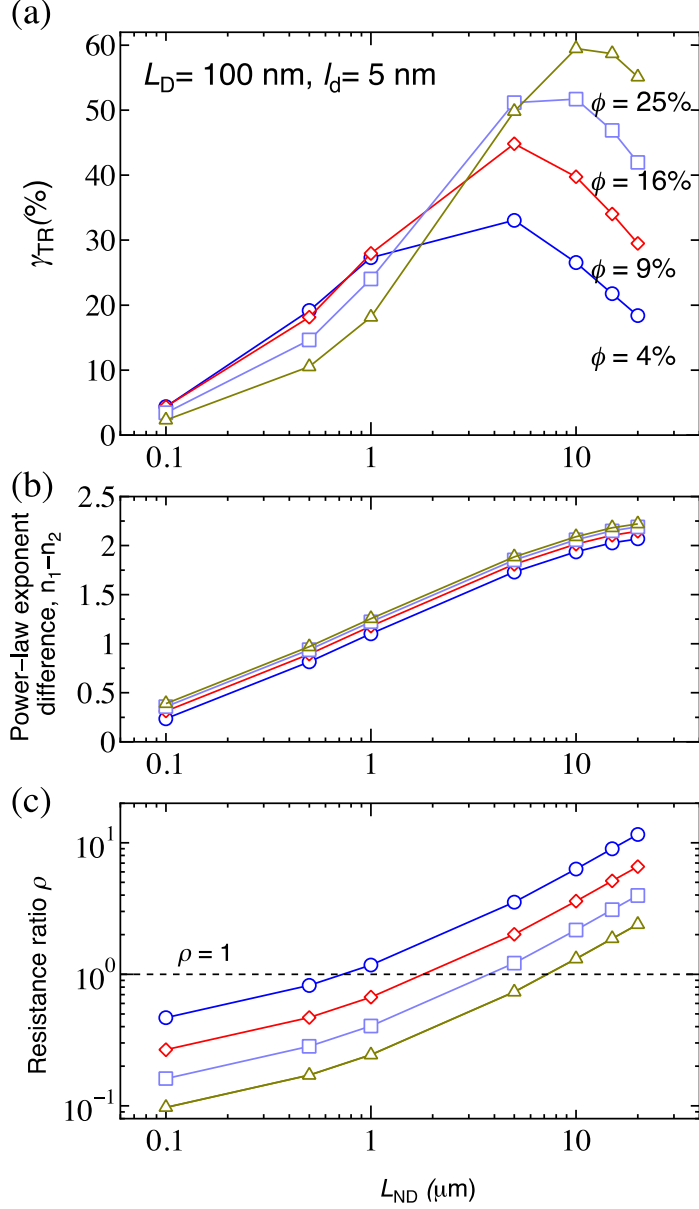


Fig. 6 (a) Thermal rectification ratio (γ_{TR}) as a function of length of non-defective graphene (L_{ND}) with different volume percentages of defects (ϕ) obtained by IS analysis, with inputs from Monte Carlo (MC) simulations. In this calculation, the length of defective graphene (L_D) and size of cubic defect (l_d) are set to 100 nm and 5 nm, respectively. Hot and cold temperatures are 500 K and 200 K (namely mean temperature T_0 is 350 K). (b) and (c) power-law exponent difference ($n_1 - n_2$) and resistance ratio (ρ) as a function of L_{ND} with different ϕ corresponding to (a). Here n_1 and n_2 are power law exponents of defective and non-defective graphenes.

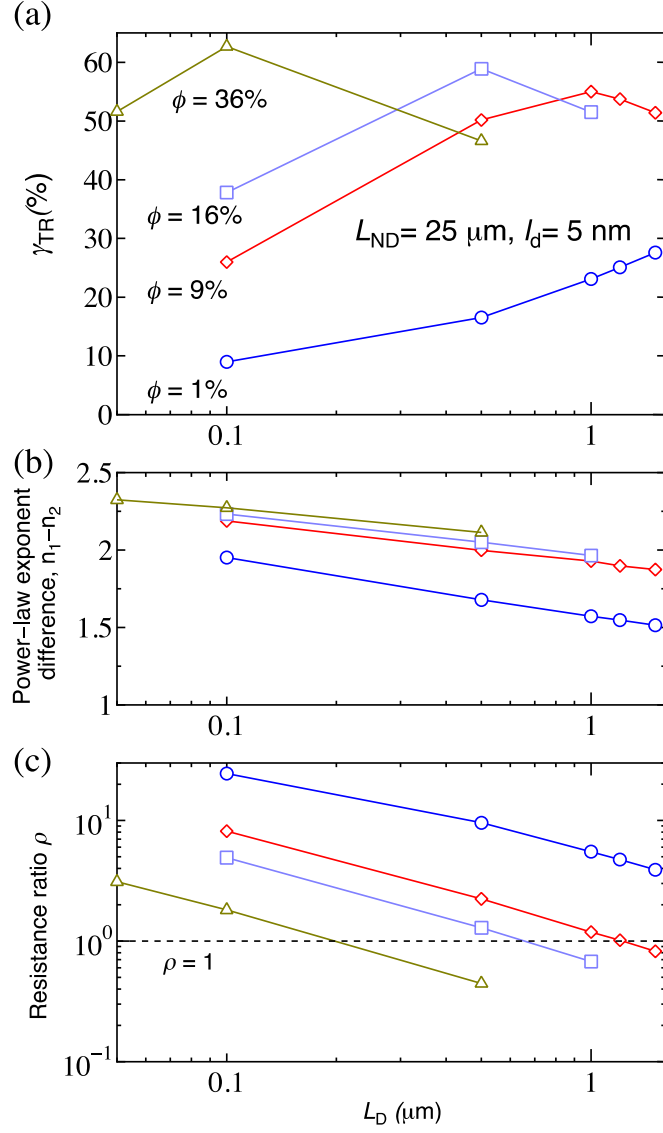


Fig. 7 (a) γ_{TR} as a function of length of defective graphene (L_D) with different ϕ obtained by IS analysis, with inputs from MC simulations. In this calculation, the length of non-defective graphene (L_{ND}) and size of cubic defect (l_d) are set to $25 \mu\text{m}$ and 5 nm , respectively. Hot and cold temperatures are 500 K and 200 K (namely mean temperature T_0 is 350 K). (b) and (c) power-law exponent difference ($n_1 - n_2$) and resistance ratio (ρ) as a function of L_D with different ϕ corresponding to (a). Here n_1 and n_2 are power law exponents of defective and non-defective graphenes.

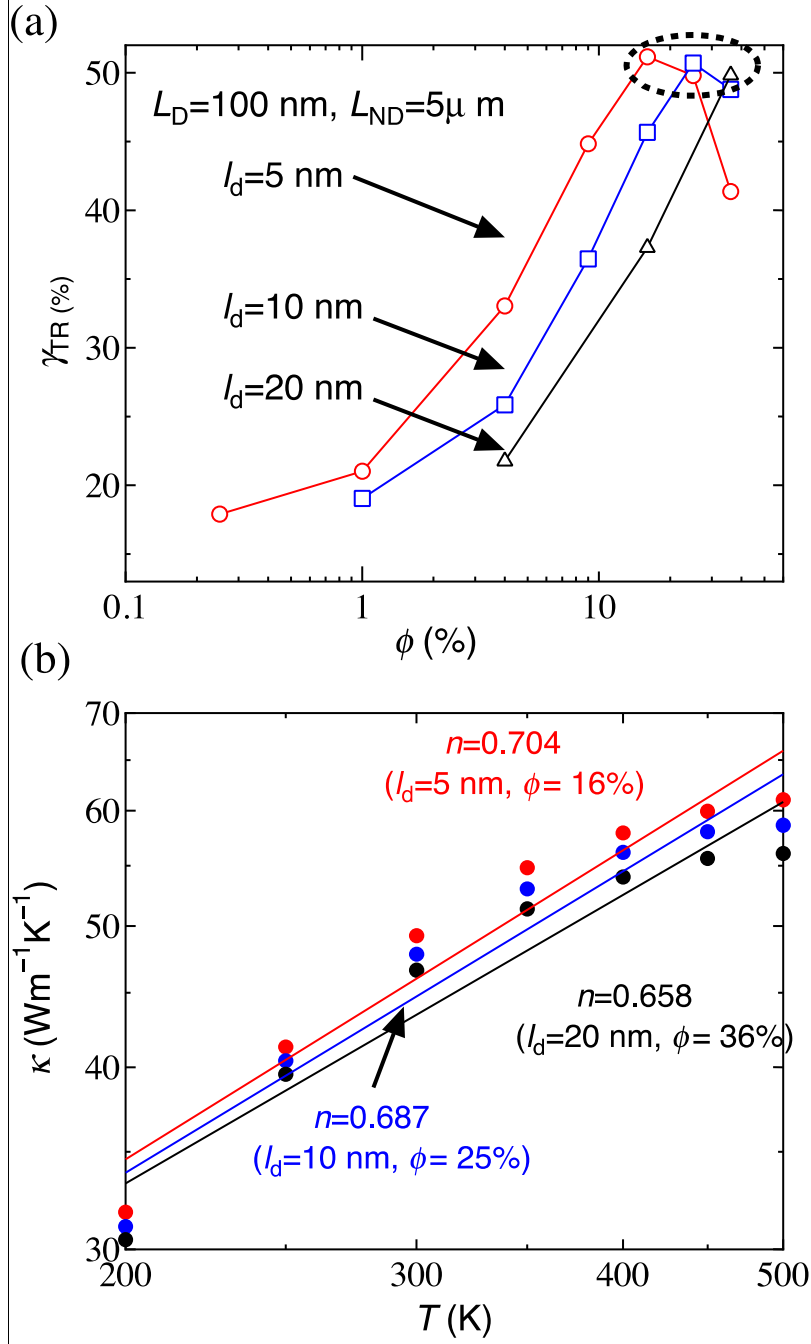


Fig. 8 (a) ϕ -dependent γ_{TR} for different l_d . L_{ND} and L_D are fixed as $5 \mu\text{m}$ and 100 nm, respectively. (b) Temperature-dependent κ for the defective side corresponding to γ_{TR}^{\max} (encircled) in (a). L_D is fixed as 100 nm. Solid lines indicate power-law fitting of κ with respect to temperature, and n denotes the power law exponent for the fitting.

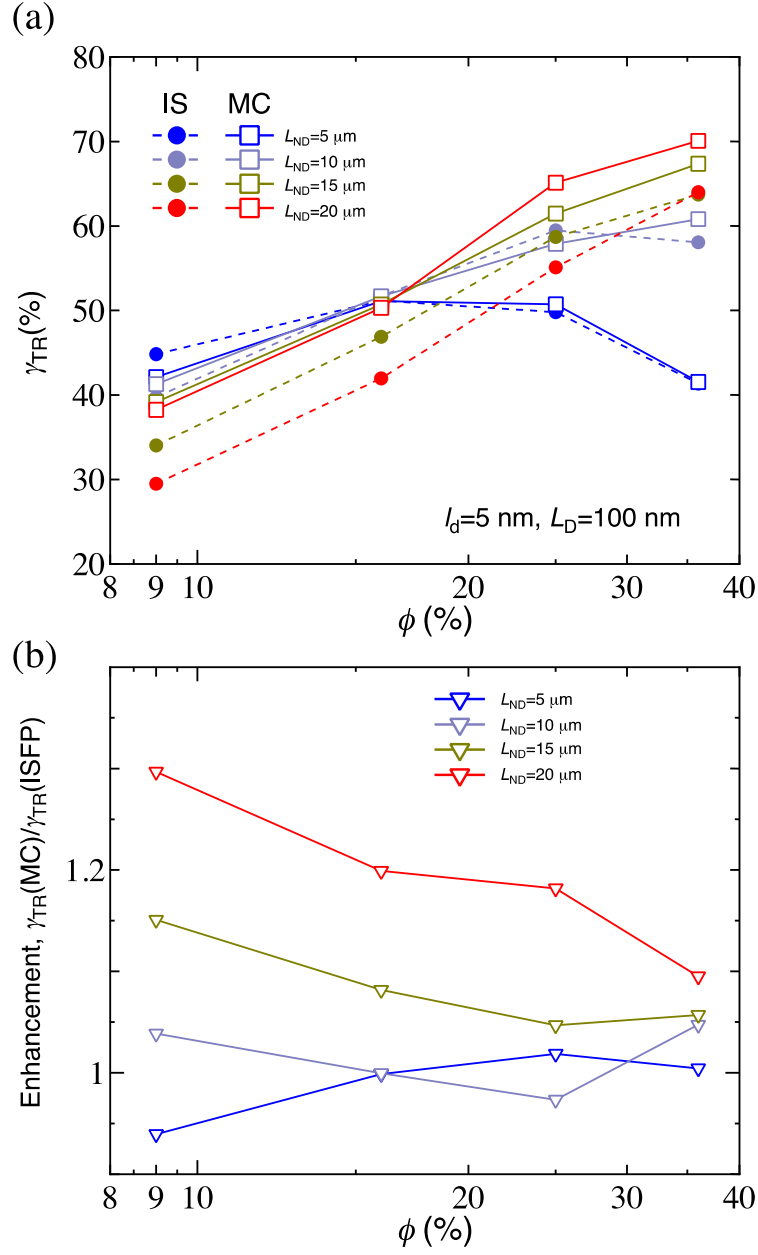


Fig. 9 (a) ϕ -dependent γ_{TR} of restructured graphene from IS analysis and full-MC simulations. γ_{TR}^{IS} and γ_{TR}^{MC} represent γ_{TR} calculated by IS approach and full-MC simulation, respectively. (b) Enhancement of thermal rectification ratio, $\gamma_{TR}^{MC} / \gamma_{TR}^{IS}$.

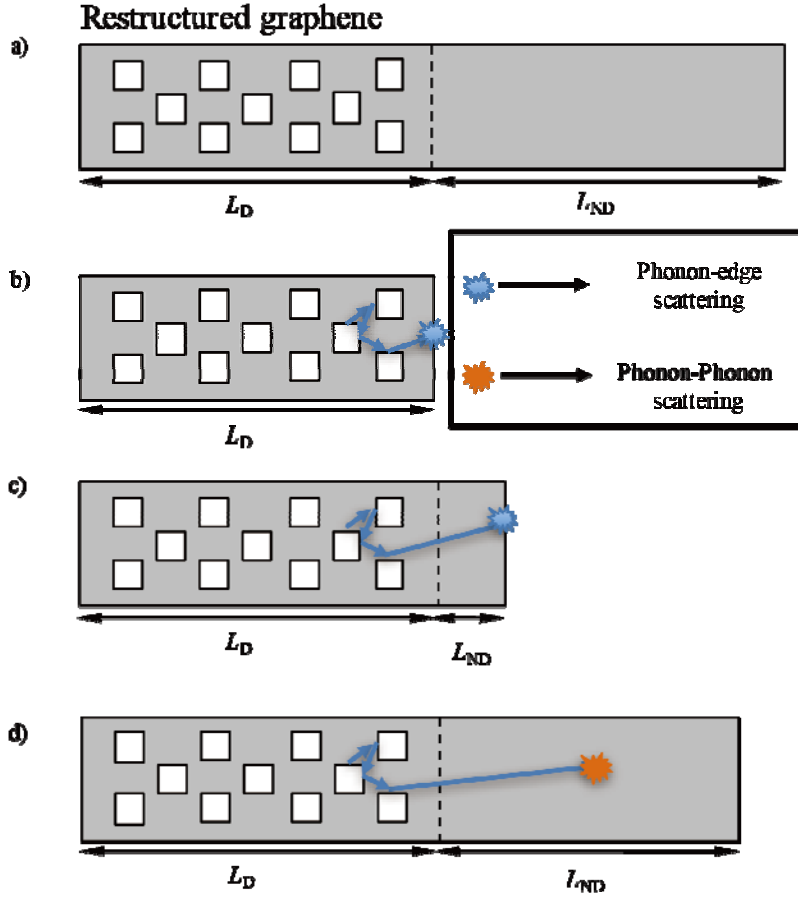


Fig. 10 Schematic showing the change in phonon dynamics, near the interface region, with the addition of a non-defective portion to a defective graphene. a) Restructured system consisting of both a defective and a non-defective region, b) phonon interacts with the system edge and undergoes phonon-edge scattering, c) with the addition of a short non-defective side (almost all the phonons have longer MFP than L_{ND}), most of the phonons still interact directly with the system edge, d) larger L_{ND} reduces this interaction for the phonons with MFP less than L_{ND} , leading to a reduced non-equilibrium in phonon distribution.